MOX-Report No. 58/2023

Personalized pressure conditions and calibration for a predictive computational model of coronary and myocardial blood flow

Montino Pelagi, G.; Baggiano, A.; Regazzoni, F.; Fusini, L.; Alì, M.; Pontone, G.; Valbusa, G.; Vergara, C.

MOX, Dipartimento di Matematica
Politecnico di Milano, Via Bonardi 9 - 20133 Milano (Italy)

mox-dmat@polimi.it https://mox.polimi.it

Personalized pressure conditions and calibration for a predictive computational model of coronary and myocardial blood flow

Giovanni Montino Pelagi[1], Andrea Baggiano[2,3], Francesco Regazzoni[4], Laura Fusini[2], Marco Alì[5,6], Gianluca Pontone[2,7], Giovanni Valbusa[5] and Christian Vergara[1]

[1]Dipartimento di Chimica, Materiali e Ingegneria Chimica "Giulio Natta", Politecnico di Milano, Piazza Leonardo da Vinci 32, Milan, 20133, Italy.
[2]Perioperative Cardiology and Cardiovascular Imaging Department, Centro Cardiologico Monzino IRCCS, Via Carlo Parea 4, Milan, 20138, Italy.
[3]Department of Clinical Sciences and Community Health, University of Milan, Milan, Italy.
[4]MOX, Dipartimento di Matematica, Politecnico di Milano, Piazza Leonardo da Vinci 32, Milan, 20133, Italy.
[5]Bracco Imaging S.p.A., Via Caduti di Marcinelle 13, Milan, 20134, Italy.
[6]Department of Diagnostic Imaging and Stereotactic Radiosurgery, Centro Diagnostico Italiano S.p.A. Via Saint Bon 20, Milan, 20147, Italy.
[7]Department of Biomedical, Surgical and Dental Sciences, University of Milan, Milan, 20134, Italy.

Abstract

Purpose: predictive modeling of hyperemic coronary and myocardial blood flow (MBF) greatly support diagnosis and prognostic stratification of patients suffering from coronary artery disease (CAD). In this work, we propose a novel strategy, using only

readily available clinical data, to build personalized inlet conditions for coronary and MBF models and to achieve an effective calibration for their predictive application to real clinical cases. *Methods:* experimental data are used to build personalized pressure waveforms at the aortic root, representative of the hyperemic state and adapted to surrogate the systolic contraction, to be used in computational fluid-dynamics analyses. Model calibration to simulate hyperemic flow is performed in a "blinded" way, not requiring any additional exam. Coronary and myocardial flow simulations are performed in eight patients with different clinical conditions to predict *FFR* and MBF. *Results:* realistic pressure waveform are recovered for all the patients. Consistent pressure distribution, blood velocities in the large arteries, and distribution of MBF in the healthy myocardium are obtained. *FFR* results show great accuracy with a per-vessel sensitivity and specificity of 100% according to clinical threshold values. Mean MBF shows good agreement with values from stress-CTP, with lower values in patients with diagnosed perfusion defects. *Conclusion:* the proposed methodology allows us to quantitatively predict *FFR* and MBF, by the exclusive use of standard measures easily obtainable in a clinical context. This represents a fundamental step to avoid catether-based exams and stress tests in CAD diagnosis.

Keywords: coronary artery disease, fractional flow reserve, myocardial perfusion, myocardial blood flow, computational modeling, coronary pressure

1 Introduction

Coronary artery disease (CAD) represents a widespread pathological condition responsible of the largest amount of deaths worldwide. Because the most critical cases require invasive surgical procedures (e.g. revascularitazion) with many risks associated [1], prognostic stratification of CAD is of paramount importance for the definition of optimal treatment options. Within this context, the assessment of cardiac perfusion through the quantification of Myocardial Blood Flow (MBF) at the cardiac tissue level is of crucial interest [2].

In current clinical practice, the gold standard is the invasive coronary angiography (ICA) together with the measurement of the fractional flow reserve (FFR) index, a widely used and reliable predictor of the hemodynamic impact of epicardial coronary lesions [3]. However, due to the invasiveness of the procedure and the need to induce a pharmacological stress condition in the patient (hyperemia), the prescription of such exam is recommended only when strictly necessary [4]. For this reason, there is great interest in enhancing the prognostic power of non-invasive exams, such as the coronary computed tomographic angiography at rest (cCTA). This technique allows for the detection and quantification of coronary lesions with great accuracy from an anatomical standpoint [2, 5], but it does not allow to assess the hemodynamic relevance of such lesions nor their impact on the MBF. The latter can be clinically

assessed through a further CT scan in stress conditions (stress-CTP exam) with additional radiation exposure and the administration of a stressor agent.

Computational models of coronary blood flow (CBF) have been proposed as a supporting tool in prognostic stratification, performing for example a patient-specific functional analysis on top of the anatomical data extracted from cCTA images [6, 7]. The most prominent example is the HeartFlow® analysis [8], which relies on computational fluid dynamics simulations in the major coronary arteries to compute the FFR index in a non-invasive way, known as FFR_{CT}. The main challenges in the field are the prescription of accurate and personalized boundary conditions, which often require either direct clinical measures (that are usually not feasible in clinical practice) [9] or surrogate 0D models (introducing a large number of parameters that may be difficult to estimate) [8, 10], and the difficulties in evaluating lesion-specific effects on the MBF at the tissue level.

In our previous works, we proposed a multiscale framework for CBF simulations from the large arteries up to the microvasculature at the cardiac tissue level [11], in what follows referred to as *CBF-Perfusion simulations*, and its application to real clinical cases for MBF quantification [12]. The main limitation was that data from the stress-CTP exam were required for a successful calibration of the myocardial constitutive parameters and for the prescription of accurate inflow boundary conditions.

The first aim of this work is to propose a new way to build an optimized inlet boundary condition in the form of a parametrized hyperemic pressure profile over time at the aortic root. Secondly, we propose a new, "blinded" calibration procedure of the CBF-Perfusion model parameters, alternative to [12], so to avoid the use of stress-CTP data. We applied these two new tools in hyperemic CBF-Perfusion simulations of eight patients, with the aim of quantitatively predicting FFR and MBF.

2 Methods

In Section 2.1 we present the framework used to build the pressure curve, to be prescribed as inlet condition to the CBF-Perfusion model, starting from patient-specific data, whereas in Section 2.2 we discuss how to adapt it to computational models that do not include the effects of cardiac contraction. In Section 2.3 we present the data-driven parametrization of the pressure curve representative of the hyperemic state; finally, in Sections 2.4 and 2.5 we discuss the CBF-Perfusion computational model, the new "blinded" calibration strategy, and the benchmark quantities we used for validation.

2.1 Pressure waveform reconstruction

The blood pressure waveform over the cardiac cycle at the aortic root (P_{ar}) shows a characteristic shape that is the result of different physiological processes, including systolic ejection, aortic valve mechanics and compliance of the aorta. This has been taken into account in the mathematical description of

the pressure waveform by using a continuous, piecewise polynomial function of time where the various time phases are approximated by different polynomial functions inspired by the specific time evolution in that region.

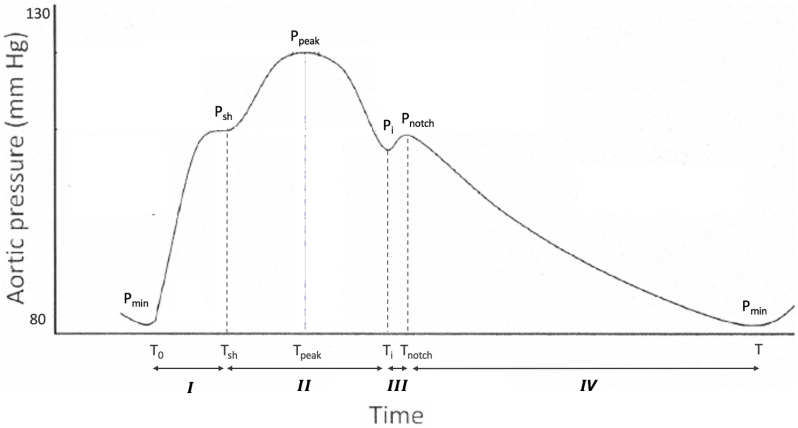

Fig. 1: Characteristic pressure waveform at the aortic root with the proposed 4-phases subdivision, key time instants and corresponding pressure values

The target waveform is subdivided into 4 regions (I-IV, see Figure 1) identified by characteristic time instants:

1. *First systolic upstroke* (I): from aortic valve opening T_0 to the systolic shoulder T_{sh}, corresponding to the peak of aortic flow velocity; approximation with a 3^{rd} order polynomial.
2. *Augmentation region* (II): from T_{sh}, through systolic peak T_{peak}, up to the incisura T_i, that is the aortic valve closure; approximation with a 2^{nd} order polynomial.
3. *Dicrotic notch region* (III): from T_i to the dicrotic notch marking the end of systole T_{notch}, taken as the end of the isovolumic relaxation phase of the ventricle; approximation with a 2^{nd} order polynomial.
4. *Diastole* (IV): from T_{notch} to the end of the cardiac cycle T; approximation with a linear polynomial.

A patient-specific parametrization of the curve is achieved through the computation of P_{ar} at the key time instants highlighted in Figure 1, using only patient's basic information and routine clinical measures, summarized in Table 1. Therefore, the procedure does not rely on invasive measures nor on exams that are not usually performed in clinical practice.

The parametrization of the four polynomials representing the pressure waveforms has been obtained as follows:

Basic information	Age Sex Height Weight
Routine clinical measures	HR heart rate P_{sys} brachial systolic pressure P_{dia} brachial diastolic pressure
Imaging-derived	left ventricular mass

Table 1: Required information for aortic pressure parametrization

I) *First systolic upstroke*: obtained through the solution of:

$$\begin{cases} P^I(t) = at^3 + bt^2 + ct + d, \\ P^I(0) = P_{min}, \\ P^I(T_{sh}) = P_{sh}, \\ \frac{\partial P^I}{\partial t}|_{t=T_{sh}} = k. \end{cases} \tag{1}$$

In problem (1), P_{min} is taken equal to P_{dia} as suggested by previous findings [13]; T_{sh} has been consistently found to occur at one third of T_{notch} for individuals over 40 years old [14]. P_{sh} can be expressed as:

$$P_{sh} = P_{peak} - \Delta P;$$

where ΔP is called the augmentation pressure, computed as follows [15]:

$$\begin{aligned} &Men: \ \Delta P/(P_{peak} - P_{min}) = \\ &\quad 79.70 + 0.63\, age - 0.002\, age^2 - 0.28\, HR - 0.39\, height_{cm}, \\ &Women: \ \Delta P/(P_{peak} - P_{min}) = \\ &\quad 56.28 + 0.90\, age - 0.005\, age^2 - 0.34\, HR - 0.24\, height_{cm}; \end{aligned}$$

Notice that, as known, P_{peak} is smaller than P_{sys} due to the increased stiffness of the distal arteries with respect to the aorta [13]. Therefore, we here set $P_{peak} = P_{sys} - 10\, mmHg$ and $P_{peak} = P_{sys} - 8\, mmHg$ for men and women, respectively [13]. Lastly, k in (1) is an empirical parameter used to improve the smoothness in the transition from time region 1 to region 2, and was set to $k = 75$ mmHg/s.

II) *Augmentation region*: obtained through the solution of:

$$\begin{cases} P^{II}(t) = a(t - T_{peak})^2 + P_{peak}, \\ P^{II}(T_{sh}) = P_{sh}. \end{cases} \tag{2}$$

T_{peak} corresponds to the time of arrival of the reflected pressure wave and it was set equal to $T_{notch}/2$ [16]. The pressure curve in this time region can then

be used to compute the pressure P_i at the incisura time T_i, which is defined as:

$$T_i = T_{notch} - IVRT,$$

where IVRT is the isovolumic relaxation time. Given that systole starts at $T_0 = 0$, T_{notch} coincides with the duration of the systolic phase and, for its computation, we here use a 2^{nd} order fitting we built on the experimental data from Bombardini et al. [17]. This method leads to the diastolic/systolic time ratio R, depending on the HR in bpm:

$$R = 2.537 * 10^{-4} \, (HR)^2 - 0.057 \, HR + 4.3,$$

which can be used to easily compute both the systolic duration T_{notch} and diastolic duration $T - T_{notch}$. Regarding the computation of IVRT, previous studies pointed out that this duration depends mainly on age and Left Ventricular Indexed Mass (LVIM) [18], so here we propose a double-regression method based on experimental data from Larrazet et al. [18], which include measures of IVRT both on a population of healthy controls of varying age (range 15-90 yrs) and on a mixed population including also patients affected by left ventricular hypertrophy (increased left ventricular mass) with a rather narrow age range (mean age 54 ± 14 yrs). The double-regression method we propose consists in the following steps:

1. Data from the healthy control group were used to build the linear regression $IVRT_{normal}$ vs age:

$$IVRT_{normal}[ms] = 0.412 \, age[y] + 47.882;$$

2. Data from the patients group were used to build the linear regression $IVRT^{54}(ms)$ vs LVIM, with the superscript "54" representing the mean age of the population and the LVIM was computed with the Du Bois formula using the subject height and weight:

$$IVRT^{54}[ms] = 0.267 \, LVIM[g/m^2] + 51.45;$$

3. The regression as in point 2 is corrected accounting for age with a shifting factor $s = 0.412 * (age - 54)$, derived from the regression described in point 1. The final double regression reads:

$$IVRT[ms] = 0.267 \, LVIM[g/m^2] + 51.45 + s.$$

III) *Dicrotic notch region*: obtained through the solution of:

$$\begin{cases} P^{III}(t) = a(t - T_{notch})^2 + P_{notch}, \\ P^{III}(T_i) = P^{II}(T_i). \end{cases} \tag{3}$$

In problem (3), we computed P_{notch} from a simplified mean pressure $P_{mean} = 0.5 * (P_{max} + P_{min})$ using a regression method we built on experimental data from Hèbert et al. [19]. The obtained regression line (R = 0.974) was:

$$P_{notch}[mmHg] = 1.1667\, P_{mean}[mmHg] - 12.629.$$

IV) *Diastole*: obtained from the solution of:

$$\begin{cases} P^{IV}(t) = mt + q, \\ P^{IV}(T_{notch}) = P_{notch}, \\ P^{IV}(T_{notch} + T) = P_{min}. \end{cases} \tag{4}$$

Summarizing, the aortic pressure waveform P_{ar} piecewise reconstructed with this method reads:

$$P_{ar}(t) = \begin{cases} P^{I} & t \in [0, T_{sh}] \\ P^{II} & t \in [T_{sh}, T_i] \\ P^{III} & t \in [T_i, T_{notch}] \\ P^{IV} & t \in [T_{notch}, T] \end{cases} \tag{5}$$

This pressure waveform can be used as an inlet boundary condition, prescribed at the coronary ostia, in any computational model of coronary circulation. However, models that do not include the effects of cardiac contraction require a special treatment that is discussed in the following section.

2.2 Adaptation to non-contracting computational models

One of the disadvantages of using a prescribed pressure inlet condition in coronary flow models (instead of a more standard prescription of the inflow over time) is that, if the effects of cardiac contraction are neglected, the higher systolic pressure produces higher flows in systole rather than diastole, which is not in accordance with the physiology of coronary circulation [20]. As experimental studies [21] pointed out, the pressure buildup inside the ventricular chamber, resulting from systolic contraction, has a major limiting effects on systolic coronary flow due to the compressive force on the microvasculature.

To take these effects into account without including a very complex and computationally expensive contraction model, we propose to correct the inlet boundary condition (5) as follows:

$$P_{eff} = P_{ar} - P^*_{LV}, \tag{6}$$

where P_{eff} represents the actual driving force of coronary flow because P^*_{LV} surrogates the effect of the pressure inside the left ventricular chamber. Since P^*_{LV} is difficult to estimate, we introduce the following assumptions:

- In the ejection phase (from T_0 to T_i), pressure in the left ventricular chamber is slightly higher than P_{ar} but its effects gradually decline moving from the

endocardium towards the epicardium. [22]. For this reason, we set $P^*_{LV} = 0.7 * P_{ar}$ as a global approximation.
- In the central phase of diastole (from the end of isovolumic relaxation up to the onset of the isovolumic contraction), ventricular pressure is negligible, so we set $P^*_{LV} = 0$.

During the isovolumic contraction and relaxation phases, P_{eff} is modeled with 2^{nd} order polynomials while ensuring continuity. In particular, during isovolumic relaxation (IR) we have:

$$\begin{cases} P^{IR}(t) = a(t - T_{notch})^2 + P_{notch}, \\ P^{IR}(T_i) = 0.3 * P_{ar}(T_i); \end{cases}$$

whereas during isovolumic contraction (IC):

$$\begin{cases} P^{IC}(t) = a(t - (T - IVCT))^2 + P_{ar}(T - IVCT), \\ P^{IC}(T) = 0.3 * P_{ar}(T), \end{cases}$$

where $IVCT = 0.05s$ is the isovolumic contraction time [23]. Summarizing, the effective pressure waveform P_{eff} piecewise reconstructed with this method reads:

$$P_{eff}(t) = \begin{cases} 0.3 * P_{ar} & t \in [0, T_i], \\ P^{IR} & t \in [T_i, T_{notch}], \\ P_{ar} & t \in [T_{notch}, T - IVCT], \\ P^{IC} & t \in [T - IVCT, T]. \end{cases}$$

From now on, the strategy to reconstruct the pressure curves P_{ar} and P_{eff} presented so far in Sections 2.1 and 2.2 will be referred to as *4-phases parametrization* technique.

2.3 Data-driven estimation of hyperemic data

For the computational simulation of drug-induced hyperemic "stress" flow, the pressure waveforms obtained as in Sections 2.1 and 2.2 have to be reparametrized so that the effects of the drugs can be taken into account. To this aim, we used a database of 100 patients with direct measures of heart rate, systolic pressure, and diastolic pressure, before and after the administration of exogenous adenosine, to build regression lines to be used for the computation of the new stress parameters starting from their "rest" counterparts:

$$X_{stress} = \alpha\, X_{rest} + \beta. \tag{7}$$

Being the database composed of clinical measures, a statistical elaboration based on interquartile range was performed first to spot and remove unreliable measures (statistical outliers). Setting X_{rest} and X_{stress} to be one of the measures of interest (heart rate or systolic/diastolic pressure) at rest and in

stress conditions, respectively, the difference $\Delta X = X_{rest} - X_{stress}$ for each record was computed. Measure records were considered reliable if:

$$[Q_1 - 0.5 * IQR] < \Delta X < [Q_3 + 0.5 * IQR] \tag{8}$$

with Q_1 and Q_3 being the first and third quartile of the distribution of ΔX, respectively, and $IQR = Q_3 - Q_1$ is the interquartile range. Indeed, values of ΔX out of the range (6) the extremities of the distribution, likely representing unreliable measures. This dataset cleaning procedure ruled out 25 of the 100 records of the dataset.

2.4 Coronary Blood Flow - Perfusion model and calibration

Hyperemic CBF-Perfusion simulations are ran using the computational model presented and used in [11, 12]. This model features a 3D description of blood fluid dynamics in the large arteries (Navier-Stokes equations, NS) and in the microcirculation (Darcy equations), suitably coupled through interface conditions representing mass conservation and forces balance. NS is solved in a detailed coronary tree resulting from a single-vessel segmentation of cCTA images. This segmentation includes the 3 main coronary arteries (Left Anterior Descending, LAD, Left Circumflex, LCX, and Right Coronary Artery, RCA) alongside their major branches up to the imaging resolution limit (minimum diameter $D_{min} \simeq 0.8\,\text{mm}$) and relies on the open-source software packages VMTK [24]. On the other side, blood dynamics in the small arteries and microcirculation is though as a flow in a porous medium and accordingly solved with a homogenized Darcy problem. This is achieved through a multicompartment Darcy formulation that is solved in the left ventricle free wall [6], also segmented from rest cCTA images.

The new model setup with respect to the hyperemic state was performed at various levels:

1. Anatomic variations. Dilation of the large arteries was accounted through a uniform radial dilation by a factor of 1.225. We propose to use this factor resulting from the mean dilation of the distal RCA, as computed from direct measurements on rest and stress CT images, performed by an expert cardiologist.
2. Physiologic variations - myocardial parameters. Dilation of the microcirculatory vessels is taken into account through a calibration of the parameters of the Darcy model. Differently from what we did in [12], where we used data from the stress-CTP maps for this calibration, we here propose the following "blinded" approach. Constitutive Darcy parameters, namely the permeability of the i-th compartment K_i and conductances between compartments i-j β_{ij} (see [11] for further information) were chosen as scalar constants. Permeabilities were set to $K_i = 2 \times 10^{-9}\,\text{m}^2\,\text{Pa}^{-1}\,\text{s}^{-1}$ as previously suggested [7]. Conductances were first calibrated at rest to achieve

two targets: firstly, a total arterial inflow of $1\,\mathrm{mL\,min^{-1}\,g^{-1}}$ in patient P1, which has angiographically normal arteries. This choice was made to rule out eventual autoregulation mechanisms that may be present in pathological conditions. Secondly, the recovery of a pressure distribution, along the microvasculature, in accordance with experimental measures [25]. Stress conductances were then obtained so that the total conductance would be 4 times its resting value, as suggested by previous findings [8] and to recover the changes in the pressure distribution along the microvasculature experimentally observed in the hyperemic state [25]. Importantly, the same parameters calibrated this way on patient P1 were used also for all the other patients P2-P8 and represent therefore the first viable approach towards a predictive application.

The final geometry of the large coronaries was meshed with radius-dependent tetrahedral elements, while the left ventricle free wall was meshed with uniform hexahedral elements, as reported in Figure 2 for patient P7. Numerical treatment of the convective term in the Navier-Stokes equations, quantities related to blood rheology (Newtonian) and other numerical quantities (time step, tolerances, solution algorithms, preconditioners etc.) were the same as previously used in [12]. CBF-Perfusion simulations were run using the software `life`^{x}, a high performance library for finite element simulations of multiphysics, multiscale and multidomain problems developed at MOX - Dipartimento di Matematica - Politecnico di Milano, within the iHEART project [26].

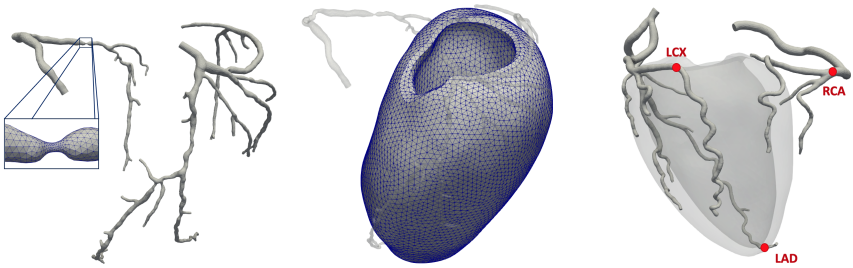

(a) (b) (c)

Fig. 2: a-b) Segmented domains and meshes for patient P7 used for the simulations of 3D blood fluid dynamics (a) and multicompartment Darcy (b) problems. c) Landmarks on the coronary tree used for the computation of FFR values for patient P2 (shown as an example of left coronary dominance). Notice that the landmark for RCA is placed earlier than the interventricular and posterior branches, and the landmark for LCX is placed earlier than the posterolateral descent

2.5 Quantities for validation

Hyperemic CBF-Perfusion simulations as described in Section 2.4 were ran in eight patients. For each of them, we have at disposal: contrast-enhanced cCTA acquisitions in resting conditions, ICA and invasive FFR measures, dynamic stress Computed Tomograhic Perfusion (stress-CTP) maps with quantitative information on myocardial blood flow (MBF) under stress conditions. Table 2 reports a summary of each patient's clinical condition; for each of the above quantities, a suitable score is assigned.

Patient ID	ICA	FFR	stress-CTP
P1	0	0	0
P2	0	0	0
P3	1	0	0
P4	1	0	0
P5	3	2	3
P6	2	2	2
P7	3	3	3
P8	2	2	2

Table 2: Clinical score of the patients population. Each score refers to the number of major coronary arteries (among LAD, LCX and RCA) having a positive outcome of the corresponding exam. Score = n when: ICA - n coronaries features at least a lesion with % stenosis $> 70\%$; FFR - n coronaries with FFR index < 0.8; stress-CTP - n perfusion territories (among the three principal ones) with MBF under stress < 150 ml/min/100g

Post-processing of results and retrospective validation was performed using the outcomes of invasive FFR and stress-CTP. The FFR index in a point is formally defined as the ratio between the actual flow rate and the hypothetical flow rate that would occur in the same location in the absence of stenosis. In practice, FFR is approximated by the ratio between the measured pressure in that point and the aortic pressure. Accordingly, the in silico counterpart of the FFR index (FFR_{CT}) was computed at each time instant and over the whole coronary domain as:

$$FFR_{CT}(\boldsymbol{x}) = \frac{P(\boldsymbol{x})}{P_{inlet}}, \tag{9}$$

where P is the computed blood pressure and P_{inlet} is the pressure at the aortic root, which coincides with the prescribed boundary condition. The FFR_{CT} values are computed at specific landmarks chosen according to the clinical methodology during invasive FFR measures and reported in Figure 2-c in the case of patient P2:

- LAD: distal segment, at the ventricle apex;
- LCX: distal segment prior to the posterior descending artery, in the case of left-dominant heart (i.e. when the posterior descending branch originates from the LCX); end of LCX, otherwise;

- RCA: distal segment prior to the bifurcation into the posterior and interventricular arteries.

To ensure that the general hemodynamic conditions were actually representative of the patient's state, we computed MBF_{comp} as the average MBF (over the left ventricular volume and over the whole cardiac cycle) from the results of the simulations (see [12] for details on its definition) and then directly compared it to the MBF_{ctp}, taken as the in-space average MBF obtained from the perfusion maps given by the stress-CTP exam.

3 Results

3.1 Inlet hyperemic pressure curves

Figure 3 reports the regression lines to relate hyperemic and resting state quantities, obtained by applying the method described in Section 2.3 to the clinical dataset at disposal which includes values of HR, and systolic and diastolic pressures P_{sys} and P_{dia} (at rest and in stress conditions). In Table 3 we report, for all the three quantities of interest, the values of α and β in (7) and the corresponding correlation coefficient R. The distributions of the data highlight two effects of adenosine: a relevant increase in heart rate and a slight decrease in both systolic and diastolic blood pressures.

Figure 4 reports, for the hyperemic case, the aortic root pressure P_{ar} and the effective pressure P_{eff} curves over a cardiac cycle for the patients P1-P8, obtained with the 4-phases parametrization technique described in Section 2.

From these results, we notice that all features characterizing the aortic pressure waveform were captured by our technique, which was able to recover physiological ranges and specific morphology of the curves. Notice also that, for construction, the two curves coincides during most of diastole. Instead, during systole, P_{eff} is smaller as it is meant to surrogate the systolic impediment of flow due to the contraction.

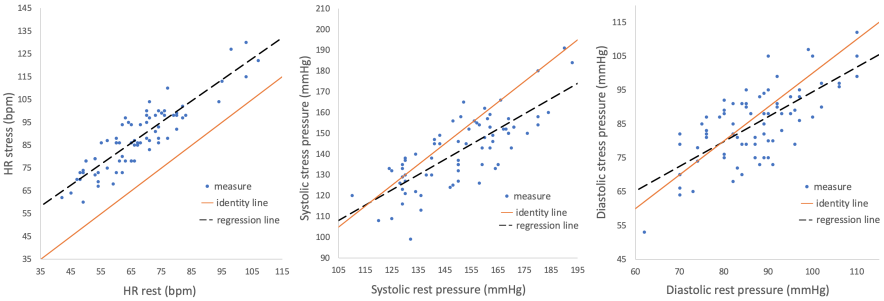

(a) (b) (c)

Fig. 3: a) Regression line built on clinical data of rest and stress heart rate measures. b-c) Regression lines built on clinical data of rest and stress systolic/diastolic pressure measures.

Parameter	α	β	R
HR bpm	0.92	26.00	0.89
P_{sys} mmHg	0.73	31.10	0.78
P_{dia} mmHg	0.73	21.25	0.70

Table 3: Coefficients and R values obtained with the rest-stress regression for the specific units of measure reported

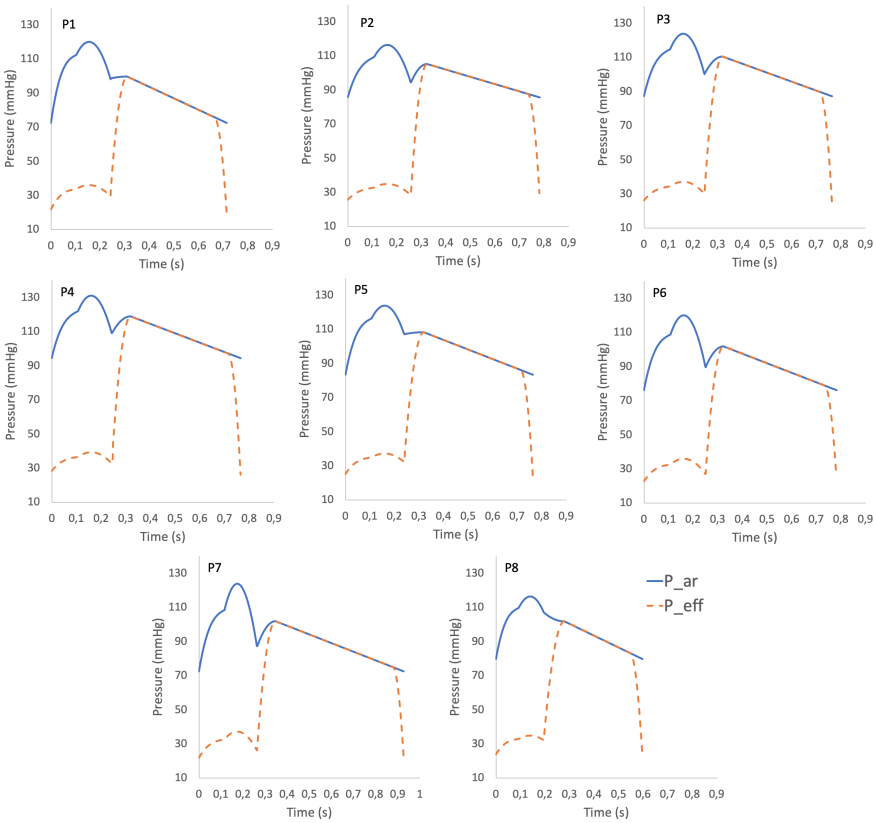

Fig. 4: Aortic root P_{ar} and effective pressure P_{eff} curves reconstructed with the 4-phases parametrization technique described in Section 2 for the patients P1-P8

3.2 Hyperemic CBF-Perfusion simulations

Figure 5 reports the computational results obtained, by means of the coupled CBF-Perfusion model, as described in Section 2.4, in the 3D coronary and myocardial domains for patient P1. In particular, we show the velocity and pressure fields in the large arteries and MBF_{comp} in the left ventricle free wall, all computed in diastole. Notice that physiological pressure, pressure gradient, and velocity magnitude are recovered along all the coronary branches. In order to highlight the recovery of the characteristic diastolic flow, we also report the computed flow rate Q at the coronary inlets. We can notice that the right coronary flow is substantially lower than the left one even if the flow subdivision has not been prescribed *a priori*. This means that the flow subdivision is regulated solely by the anatomy of the coronary tree and that our proposal for the inlet pressure condition can be used without any additional assumption.

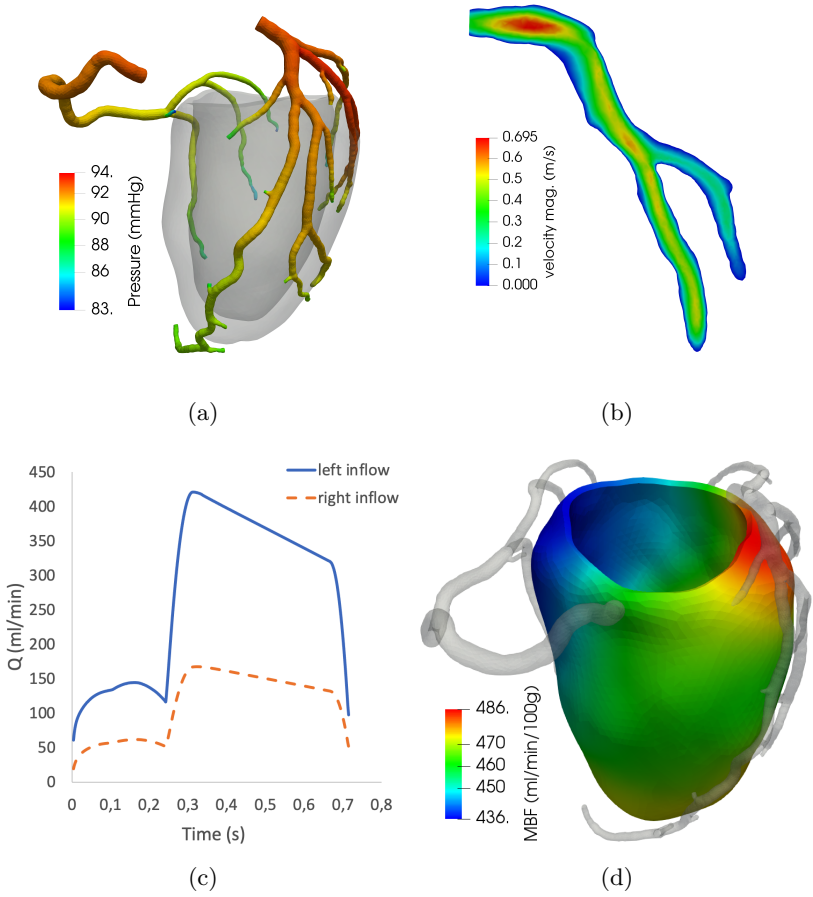

Fig. 5: a) Pressure field in the large coronaries computed at peak diastolic pressure ($t = 0.3\ s$). b) Velocity field computed at mid diastole ($t = 0.5\ s$) in the LAD; the slicing plane is aligned with the LAD centerline in the middle segment but not at the inlet. c) Left/right coronary blood flow Q computed over time at the left/right coronary inlets. d) Istantaneous myocardial blood flow (MBF) in the left ventricle free wall computed at mid diastole ($t = 0.5\,s$). Patient P1

Figure 6 reports, starting from the computational solution of the CBF-Perfusion model, the FFR_{CT} values for patients P1-P8, computed by means of (9), at the (patient-dependent) time corresponding to the peak diastolic pressure. FFR_{CT} results showed little variation in time during the diastolic phase, so we do not expect different results at other time instants. These results allow us to reproduce with great accuracy the outcomes of the invasive

FFR procedure, leading to an effective identification of functionally significant lesions characterized by $FFR < 0.8$.

In Table 4, the quantitative comparison between FFR_{CT} values and invasive FFR measures, for each major artery of each patient, is reported. According to the clinical methodology, in the case of mild ($< 30\%$) and critical ($> 90\%$) stenosis the invasive FFR measure is not performed, since in such conditions FFR is supposed to be large (> 0.8) and small, respectively. Accordingly, in such cases a negative (N) and positive (P) score is directly assigned by clinicians. In the other cases, we report the exact invasive FFR measure. We notice the excellent agreement between FFR predictions and invasive measures.

Figure 7 reports the mean value of MBF for patients P1-P8, both in space over the whole myocardium and in time over the whole cardiac cycle, compared with the values extracted from the stress-CTP maps. We notice that, in all the patients, the average MBF_{comp} is always in the physiological range for stress conditions.

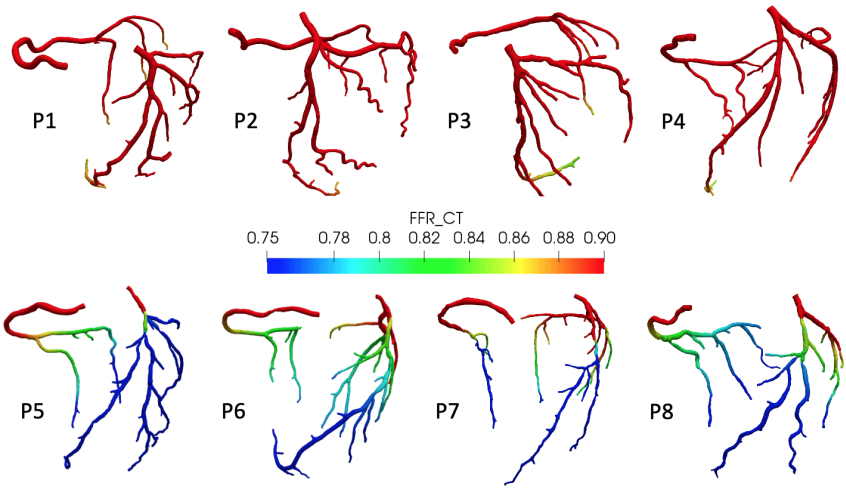

Fig. 6: FFR_{CT} results for patients P1-P8, computed at peak diastolic pressure over the whole coronary domain. Patients 5-8 have at least one major artery with positive outcome of the invasive FFR exam (invasive $FFR < 0.8$).

Patient ID	LAD	LCX	RCA
P1	0.94 – N	0.91 – N	0.96 – N
P2	0.84 – N	0.90 – N	0.97 – N
P3	0.90 – 0.88	0.96 – 0.96	0.95 – N
P4	0.92 – N	0.96 – N	0.97 – 0.95
P5	0.49 – P	0.55 – P	0.90 – 0.84
P6	0.65 – P	0.75 – P	0.86 – 0.91
P7	0.40 – P	0.50 – P	0.35 – P
P8	0.64 – P	0.88 – N	0.78 – N/A

Table 4: FFR results: quantitative comparison in the form: FFR_{CT} – invasive FFR, at specific landmarks of each major coronary artery (LAD, LCX, RCA). N means negative FFR outcome (stenosis degree $< 30\%$), P means positive FFR outcome (stenosis degree $> 90\%$)

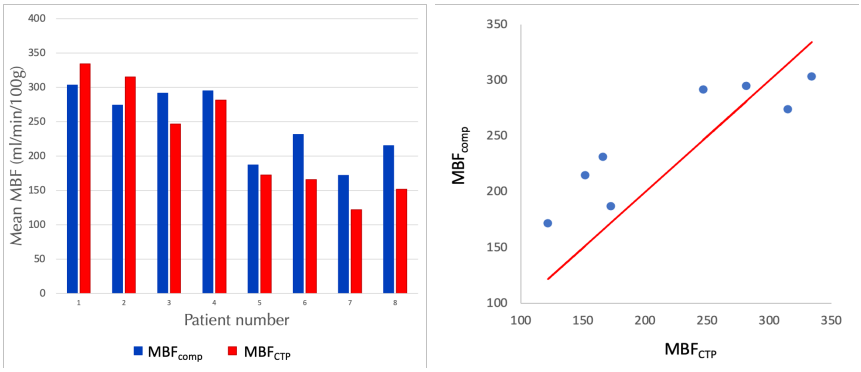

Fig. 7: Quantitative comparison between computed MBF_{comp} vs clinical MBF_{ctp} values of myocardial blood flow in patients 1-8. Patients 4-8 have at least a principal perfusion territory with positive outcome of the stress-CTP exam ($MBF_{ctp} < 150\, ml/min/100g$)

4 Discussion

In the context of prognostic stratification of Coronary Artery Disease, the assessment of coronary flow and myocardial perfusion in an hyperemic state is of crucial importance. Maximal hyperemia leads to the exhaustion of the autoregulation mechanisms of the coronary circulation, which in the case of severe pathological conditions may not be able to keep up with the augmented metabolic demand of the cardiac muscle, resulting in major adverse events. Indeed, several clinical studies have shown a high predictive value of FFR and hyperemic MBF with respect to the most commonly used clinical endpoints (major adverse event, need for hospitalization/surgical intervention) [2, 3, 5].

Within the context of predictive computational analysis of hyperemic flow, the prescription of accurate inlet conditions at the coronary ostia is a daunting task. Direct measures of coronary inflow at rest are usually not available and, even when they are, its knowledge does not allow to estimate the inflow in

the hyperemic state. Using a constant pressure inlet condition, for example the mean arterial pressure, is also not ideal because of the well-known flow impeding effect that occurs in systole due to cardiac contraction. Instead, the prescription of a pressure waveform over time would allow the modeling of the effects of cardiac contraction as a surrogate and, thus, represents an ideal solution. Nonetheless, this choice introduces many challenges, namely building the full waveform over time at the coronary ostia starting from istantaneous brachial measures and the estimation of the modifications occurring in the hyperemic state.

In this work, we propose a novel strategy to build, along the whole heartbeat, the pressure waveform at the aortic root in the two physiological states of rest and hyperemia. Notably, this strategy needs in any case only readily available clinical measures of heart rate and maximum/minimum brachial pressure at rest. The use of such waveforms as inlet boundary conditions for CBF-Perfusion simulations, together with a novel model calibration strategy that does not rely on any invasive measure, allowed us to obtain clinically meaningful results in eight patients, showing a high predictive power with respect to the FFR index and MBF.

Our computational results show that the proposed framework is able to reproduce all the characteristic features of the coronary circulation: a physiological pressure gradient along the major arteries (a), mean velocities consistent with previous, direct measurements of coronary flow [27] (b), a mostly diastolic rather than systolic flow over the cardiac cycle (c) and a reasonable MBF distribution, with local heterogeneities in accordance with the direct observations for non-ischemic myocardium [28], showing the highest local MBF values in the anterolateral wall and the lowest in the posterior wall. As it can be seen in Figure 5-c, the characteristic diastolic flow is obtained also in the right coronary artery, where it is known that, due to the lower pressure generated in the right ventricular chamber, systolic and diastolic flows are rather similar [27]. This is most likely caused by the absence, in our model, of branches perfusing the right ventricle. The definition of P_{eff} proposed in (6) would need to be refined to take this effect into account. However, we point out that this effect does not have any impact on FFR, since it is measured during diastole, nor on MBF in the left ventricle, which is largely the most clinically relevant.

From the FFR_{CT} results reported in Figure 6 and Table 4, we can see that our approach shows a high predictive power when applied to the patient-specific calculation of the FFR index for each major artery of each patient, successfully identifying functionally relevant lesions. Clustering the results following the clinical threshold of functional relevance when $FFR < 0.8$, we obtained a per-vessel sensitivity and specificity of 100%. The mean relative error computed from Table 4 was 3.4%, although such quantitative comparison is based on a rather small number of vessels compared to the total. Validation with a larger database of patients would further improve the consistency of these results.

Most importantly, from the results of Figure 7 we see that we could achieve a good accordance also for the mean MBF, especially in the non-ischemic cases (patients 1-4) where we report a mean error of 11.3%. This is especially relevant because no assumptions or data are provided to the model regarding the flow. For patients 5-8, where perfusion defects were present, we see a slight yet systematic overestimation in MBF, with a mean error of 32.6%. We hypothesize that this could be caused by two reasons: a) an underestimation of stenosis severity in the phase of geometry reconstruction, b) an underestimation of the effect of ventricular hypertrophy on diastolic flow. Patients 5, 7 and 8 showed varying degrees of left ventricular hypertrophy, which has been found to hamper diastolic flow due to the rarefaction of blood vessels in the thickened muscle [29] and the augmented compression forces on the microvasculature also in diastole [30]. Since this second effect is not included in our model, we believe that it could be the cause of the observed MBF overestimation for these patients. For patient 6, without ventricular hypertrophy, the most likely reason is an underestimation of stenosis severity, given also the relatively high values of FFR_{CT} for this patient.

Previous works in computational modeling of coronary blood flow and myocardial perfusion have focused mainly on single aspects such as FFR computation [8, 31] or the recovery of physiological flow patterns in the microcirculation through complex poroelastic models [6, 32]. This work is one of the first attempts to run a computational analysis of coronary blood flow, on real patients data with various pathologies, with a clear predictive purpose with respect to both FFR index and MBF. To the best of our knowledge, it is also the first time doing so using a full pressure waveform as inlet condition in the hyperemic state. Compared to other solutions (e.g. the use of a constant pressure [7]), this choice opens up interesting possibilities for the investigation of specific pathologies such as ventricular hypertrophy, aortic valve stenosis, augmented arterial stiffness and, in general, every condition that may alter the shape of the pressure waveform without significantly affecting its mean value.

The study presented in this work has some limitations:

- The dispersion in the clinical data regarding rest-stress pressure values is rather high. A covariate analysis with more clinical parameters may improve the consistency of the method;
- Although different clinical conditions were included in the patients population, more cases are required to improve the consistency of the results;
- A direct validation, using invasively measured pressure recordings, would provide a solid benchmark for the absolute accuracy of the proposed strategy.

Declarations

Conflict of interest: No conflicts of interest, financial or otherwise, are declared by the authors.

Ethical approval: Ethical review board gave approval for this study, and informed consent was obtained from all patients.

References

[1] Neumann, F.-J., Sousa-Uva, M., Ahlsson, A., Alfonso, F., Banning, A.P., Benedetto, U., Byrne, R.A., Collet, J.-P., Falk, V., Head, S.J., Jüni, P., Kastrati, A., Koller, A., Kristensen, S.D., Niebauer, J., Richter, D.J., Seferović, P.M., Sibbing, D., Stefanini, G.G., Windecker, S., Yadav, R., Zembala, M.O., Group, E.S.D.: 2018 ESC/EACTS Guidelines on myocardial revascularization. European Heart Journal **40**(2), 87–165 (2018) https://academic.oup.com/eurheartj/article-pdf/40/2/87/29005222/ehy394.pdf. https://doi.org/10.1093/eurheartj/ehy394

[2] Pontone, G., Rossi, A., Guglielmo, M., Dweck, M.R., Gaemperli, O., Nieman, K., Pugliese, F., Maurovich-Horvat, P., Gimelli, A., Cosyns, B., Achenbach, S.: Clinical applications of cardiac computed tomography: a consensus paper of the European Association of Cardiovascular Imaging—part I. European Heart Journal - Cardiovascular Imaging **23**(3), 299–314 (2022) https://academic.oup.com/ehjcimaging/article-pdf/23/3/299/42571532/jeab293.pdf. https://doi.org/10.1093/ehjci/jeab293

[3] De Bruyne, B., Pijls, N.H.J., Kalesan, B., Barbato, E., Tonino, P.A.L., Piroth, Z., Jagic, N., Möbius-Winkler, S., Rioufol, G., Witt, N., Kala, P., MacCarthy, P., Engström, T., Oldroyd, K.G., Mavromatis, K., Manoharan, G., Verlee, P., Frobert, O., Curzen, N., Johnson, J.B., Jüni, P., Fearon, W.F.: Fractional flow reserve–guided pci versus medical therapy in stable coronary disease. New England Journal of Medicine **367**(11), 991–1001 (2012) https://doi.org/10.1056/NEJMoa1205361. https://doi.org/10.1056/NEJMoa1205361. PMID: 22924638

[4] Knuuti, J., Wijns, W., Saraste, A., Capodanno, D., Barbato, E., Funck-Brentano, C., Prescott, E., Storey, R.F., Deaton, C., Cuisset, T., Agewall, S., Dickstein, K., Edvardsen, T., Escaned, J., Gersh, B.J., Svitil, P., Gilard, M., Hasdai, D., Hatala, R., Mahfoud, F., Masip, J., Muneretto, C., Valgimigli, M., Achenbach, S., Bax, J.J., Group, E.S.D.: 2019 ESC Guidelines for the diagnosis and management of chronic coronary syndromes: The Task Force for the diagnosis and management of chronic coronary syndromes of the European Society of Cardiology (ESC). European Heart Journal **41**(3), 407–477 (2019) https://academic.oup.com/eurheartj/article-pdf/41/3/407/32651471/ehz425.pdf. https://doi.org/10.1093/eurheartj/ehz425

[5] Pontone, G., Rossi, A., Guglielmo, M., Dweck, M.R., Gaemperli, O., Nieman, K., Pugliese, F., Maurovich-Horvat, P., Gimelli, A., Cosyns,

B., Achenbach, S.: Clinical applications of cardiac computed tomography: a consensus paper of the European Association of Cardiovascular Imaging—part II. European Heart Journal - Cardiovascular Imaging **23**(4), 136–161 (2022) https://academic.oup.com/ehjcimaging/article-pdf/23/4/e136/46425600/jeab292.pdf. https://doi.org/10.1093/ehjci/jeab292

[6] Lee, J., Cookson, A., Chabiniok, R., Rivolo, S., Hyde, E., Sinclair, M., Michler, C., Sochi, T., Smith, N.: Multiscale Modelling of Cardiac Perfusion, vol. 14. (2015). https://doi.org/10.1007/978-3-319-05230-4_3

[7] Papamanolis, L., Kim, H.J., Jaquet, C., Sinclair, M., Schaap, M., Danad, I., van Diemen, P., Knaapen, P., Najman, L., Talbot, H., Taylor, C.A., Vignon-Clementel, I.: Myocardial Perfusion Simulation for Coronary Artery Disease: A Coupled Patient-Specific Multiscale Model. Annals of Biomedical Engineering **49**, 1432–1447 (2021). https://doi.org/10.1007/s10439-020-02681-z

[8] Taylor, C.A., Fonte, T.A., Min, J.K.: Computational fluid dynamics applied to cardiac computed tomography for noninvasive quantification of fractional flow reserve: Scientific basis. Journal of the American College of Cardiology **61**(22), 2233–2241 (2013). https://doi.org/10.1016/j.jacc.2012.11.083

[9] Lodi Rizzini, M., Candreva, A., Chiastra, C., Gallinoro, E., Calò, K., D'Ascenzo, F., De Bruyne, B., Mizukami, T., Collet, C., Gallo, D., Morbiducci, U.: Modelling coronary flows: impact of differently measured inflow boundary conditions on vessel-specific computational hemodynamic profiles. Computer Methods and Programs in Biomedicine **221**, 106882 (2022). https://doi.org/10.1016/j.cmpb.2022.106882

[10] Kim, H.J., Vignon-Clementel, I., Coogan, J., Figueroa, C., Jansen, K., Taylor, C.: Patient-specific modeling of blood flow and pressure in human coronary arteries. Annals of biomedical engineering **38**(10), 3195–3209 (2010)

[11] Gregorio, S.D., Fedele, M., Pontone, G., Corno, A.F., Zunino, P., Vergara, C., Quarteroni, A.: A computational model applied to myocardial perfusion in the human heart: From large coronaries to microvasculature. Journal of Computational Physics **424**, 109836 (2021). https://doi.org/10.1016/j.jcp.2020.109836

[12] Di Gregorio, S., Vergara, C., Pelagi, G.M., Baggiano, A., Zunino, P., Guglielmo, M., Fusini, L., Muscogiuri, G., Rossi, A., Rabbat, M.G., Quarteroni, A., Pontone, G.: Prediction of myocardial blood flow under stress conditions by means of a computational model. European Journal of Nuclear Medicine and Molecular Imaging **49**(6), 1894–1905 (2022).

https://doi.org/10.1007/s00259-021-05667-8

[13] Mceniery, C., Cockcroft, J., Roman, M., Franklin, S., Wilkinson, I.: Central blood pressure: Current evidence and clinical importance. European heart journal **35** (2014). https://doi.org/10.1093/eurheartj/eht565

[14] Garcia, J., van der Palen, R.L.F., Bollache, E., Jarvis, K., Rose, M.J., Barker, A.J., Collins, J.D., Carr, J.C., Robinson, J., Rigsby, C.K., Markl, M.: Distribution of blood flow velocity in the normal aorta: Effect of age and gender. Journal of Magnetic Resonance Imaging **47**(2), 487–498 (2018) https://onlinelibrary.wiley.com/doi/pdf/10.1002/jmri.25773. https://doi.org/10.1002/jmri.25773

[15] Jeroncic, A., Gunjaca, G., Budimir Mršić, D., Mudnic, I., Brizić, I., Polasek, O., Boban, M.: Normative equations for central augmentation index: Assessment of inter-population applicability and how it could be improved. Scientific Reports **6**, 27016 (2016). https://doi.org/10.1038/srep27016

[16] Ishizaka, S., Iwano, H., Motoi, K., Chiba, Y., Tsujinaga, S., Tanemura, A., Murayama, M., Nakabachi, M., Yokoyama, S., Nishino, H., Okada, K., Kaga, S., Kamiya, K., Nagai, T., Anzai, T.: Influence of left ventricular systolic dysfunction on occurrence of pulsus tardus in patients with aortic stenosis. Journal of Cardiology **78**(4), 322–327 (2021). https://doi.org/10.1016/j.jjcc.2021.04.009

[17] Bombardini, T., Sicari, R., Bianchini, E., Picano, E.: Abnormal shortened diastolic time length at increasing heart rates in patients with abnormal exercise-induced increase in pulmonary artery pressure. Cardiovascular ultrasound **9**, 36 (2011). https://doi.org/10.1186/1476-7120-9-36

[18] Larrazet, F., Pellerin, D., Fournier, C., Witchitz, S., Veyrat, C.: Right and left isovolumic ventricular relaxation time intervals compared in patients by means of a single-pulsed doppler method. Journal of the American Society of Echocardiography **10**(7), 699–706 (1997). https://doi.org/10.1016/S0894-7317(97)70111-1

[19] He´bert, J.-L., Lecarpentier, Y., Zamani, K., Coirault, C., Daccache, G., Chemla, D., Wuilliez, N., Larsonneur, L.: Relation between aortic dicrotic notch pressure and mean aortic pressure in adults. The American Journal of Cardiology **76**(4), 301–306 (1995). https://doi.org/10.1016/S0002-9149(99)80086-1

[20] Chilian, W.M., Marcus, M.L.: Phasic coronary blood flow velocity in intramural and epicardial coronary arteries. Circulation Research **50**(6), 775–781 (1982) https://www.ahajournals.org/doi/pdf/10.1161/01.RES.50.6.775.

https://doi.org/10.1161/01.RES.50.6.775

[21] Kresh JY, B.S. Cobanoglu MA: The intramyocardial pressure: a parameter of heart contractility. J Heart Transplant (1985)

[22] Baird, R.J., Manktelow, R.T., Shah, P.A., Ameli, F.M.: Intramyocardial pressure: A study of its regional variations and its relationship to intraventricular pressure. The Journal of Thoracic and Cardiovascular Surgery **59**(6), 810–823 (1970). https://doi.org/10.1016/S0022-5223(19)42402-1

[23] Hirschfeld, S., Meyer, R., Korfhagen, J., Kaplan, S., Liebman, J.: The isovolumic contraction time of the left ventricle. an echographic study. Circulation **54**(5), 751–756 (1976). https://doi.org/10.1161/01.CIR.54.5.751

[24] Antiga, L., Piccinelli, M., Botti, L., Ene-Iordache, B., Remuzzi, A., Steinman, D.A.: An image-based modeling framework for patient-specific computational hemodynamics. Medical & Biological Engineering & Computing **46**, 1097–1112 (2008)

[25] Chilian, W.M., Layne, S.M., Klausner, E.C., Eastham, C.L., Marcus, M.L.: Redistribution of coronary microvascular resistance produced by dipyridamole. American Journal of Physiology-Heart and Circulatory Physiology **256**(2), 383–390 (1989). https://doi.org/10.1152/ajpheart.1989.256.2.H383. PMID: 2492768

[26] Africa, P.C.: lifex: A flexible, high performance library for the numerical solution of complex finite element problems. SoftwareX **20**, 101252 (2022). https://doi.org/10.1016/j.softx.2022.101252

[27] Marcus, J., Smeenk, H., Kuijer, J., Van der Geest, R., Heethaar, R., Van Rossum, A.: Flow profiles in the left anterior descending and the right coronary artery assessed by mr velocity quantification: effects of through-plane and in-plane motion of the heart. J Comput Assist Tomogr **23(4)**, 567–76 (1999). https://doi.org/10.1097/00004728-199907000-00017

[28] Chareonthaitawee, P., Kaufmann, P., Rimoldi, O., Camici, P.: Heterogeneity of resting and hyperemic myocardial blood flow in healthy humans. Cardiovascular research **50**, 151–61 (2001). https://doi.org/10.1016/S0008-6363(01)00202-4

[29] Mohammed, S., Hussain, S., Mirzoyev, S., Edwards, W., Maleszewski, J., Redfield, M.: Coronary microvascular rarefaction and myocardial fibrosis in heart failure with preserved ejection fraction. Circulation **131** (2014). https://doi.org/10.1161/CIRCULATIONAHA.114.009625

[30] Knaapen, P., Germans, T., Camici, P.G., Rimoldi, O.E., ten Cate, F.J.,

ten Berg, J.M., Dijkmans, P.A., Boellaard, R., van Dockum, W.G., Götte, M.J.W., Twisk, J.W.R., van Rossum, A.C., Lammertsma, A.A., Visser, F.C.: Determinants of coronary microvascular dysfunction in symptomatic hypertrophic cardiomyopathy. American Journal of Physiology-Heart and Circulatory Physiology **294**(2), 986–993 (2008). https://doi.org/10.1152/ajpheart.00233.2007. PMID: 18156203

[31] Xi, X., Liu, J., Sun, H., Xu, K., Wang, X., Zhang, L., Du, T., Liu, J., Li, B.: Accurate calculation of ffr based on a physics-driven fluid-structure interaction model. Frontiers in Physiology **13** (2022). https://doi.org/10.3389/fphys.2022.861446

[32] Chapelle, D., Gerbeau, J.-F., Sainte-Marie, J., Vignon-Clementel, I.: A poroelastic model valid in large strains with applications to perfusion in cardiac modeling. Computational Mechanics **46**, 91–101 (2009). https://doi.org/10.1007/s00466-009-0452-x

MOX Technical Reports, last issues

Dipartimento di Matematica
Politecnico di Milano, Via Bonardi 9 - 20133 Milano (Italy)

57/2023 Regazzoni, F.
An optimally convergent Fictitious Domain method for interface problems

55/2023 Orlando, G; Barbante, P.F.; Bonaventura, L.
On the evolution equations of interfacial variables in two-phase flows

54/2023 Orlando, G.
An implicit DG solver for incompressible two-phase flows with an artificial compressibility formulation

53/2023 Rossi, A.; Cappozzo, A.; Ieva, F.
Functional Boxplot Inflation Factor adjustment through Robust Covariance Estimators

52/2023 Antonietti, P.F.; Botti, M.; Mazzieri, I.
A space-time discontinuous Galerkin method for coupled poroelasticity-elasticity problems

51/2023 Bucelli, M.; Regazzoni, F.; Dede', L.; Quarteroni, A.
Preserving the positivity of the deformation gradient determinant in intergrid interpolation by combining RBFs and SVD: application to cardiac electromechanics

49/2023 Ieva, F.; Ronzulli, M.; Romo, J.; Paganoni, A.M.
A Spearman Dependence Matrix for Multivariate Functional Data

48/2023 Renzi, F.; Vergara, C.; Fedele, M.; Giambruno, V.; Quarteroni, A.; Puppini, G.; Luciani, G.B.
Accurate and Efficient 3D Reconstruction of Right Heart Shape and Motion from Multi-Series Cine-MRI

44/2023 Fontana, N.; Savaré, L.; Rea, F.; Di Angelantonio, E.; Ieva, F.
Long-term adherence to polytherapy in heart failure patients: a novel approach emphasising the importance of secondary prevention

45/2023 Gironi, P.; Petraro, L.; Santoni, S.; Dede', L.; Colosimo, B.M.
A Computational Model of Cell Viability and Proliferation of Extrusion-based 3D Bioprinted Constructs During Tissue Maturation Process